

Contents lists available at ScienceDirect

Materials & Design

journal homepage: www.elsevier.com/locate/matdes



Mn content optimum on microstructures and mechanical behavior of Fe-based medium entropy alloys



Yanchun Zhao ^{a,*}, Huwen Ma ^a, Linhao Zhang ^a, Dong Zhang ^c, Shengzhong Kou ^a, Bo Wang ^a, Wensheng Li ^{a,*}, Peter K. Liaw ^{b,*}

- ^a State Key Laboratory of Advanced Processing and Recycling of Non-ferrous Metals, Lanzhou University of Technology, Lanzhou 730050, PR China
- ^b Department of Materials Science and Engineering, The University of Tennessee, Knoxville, TN 37996-2200, USA
- c State Key Laboratory of Comprehensive Utilization of Nickel and Cobalt Resources of Jinchuan Group Co., Ltd., Jinchang 737100, PR China

HIGHLIGHTS

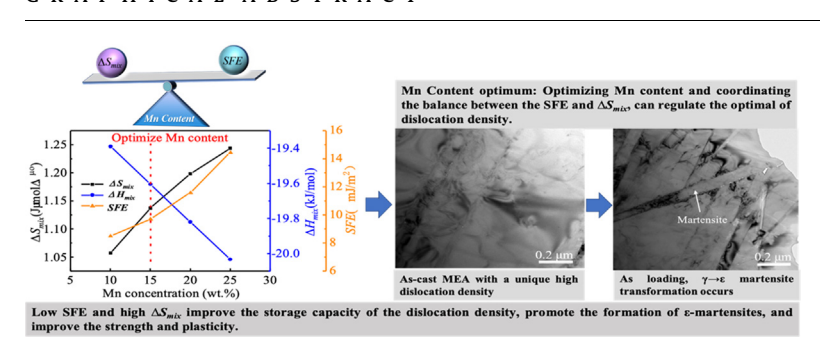
- The Medium entropy alloys possess low stacking fault energy and unique high as cast dislocation densities.
- The modified Warren-Averbach equation and the thermodynamic model are used to calculate alloy dislocation density and stacking fault.
- Low stacking fault energy and high mixing enthalpy improve storage capacity of dislocation density, promote formation of ε-martensites, and improve strength and plasticity.
- Optimizing Mn content and coordinating the balance between stacking fault energy and the mixing enthalpy, can regulate optimal dislocation density.

ARTICLE INFO

Article history:
Received 2 March 2022
Revised 27 June 2022
Accepted 6 October 2022
Available online 7 October 2022

Keywords: Medium entropy alloy Dislocation density Phase transformation Work hardening

G R A P H I C A L A B S T R A C T



ABSTRACT

Fe-XMn-5Si-10Cr-0.9C (X = 10, 15, 20, and 25 wt%) medium entropy alloys (MEAs) with different Mn contents were prepared by magnetic suspension melting in a water-cooled copper crucible, and casted in a negative pressure suction copper mould. The modified Warren-Averbach equation and the thermodynamic model were used to calculate the alloy dislocation density and stacking faults, respectively. The effects of the Mn content on the phase structure, stacking fault energy (SFE), dislocation density, and mechanical properties of the alloy were investigated. The results indicate that the MEAs possess a low stacking fault energy (\sim 8.50–14.44 mJ/m²) and a unique high as-cast dislocation density (up to 4.8 × 10¹⁵ m²). The microstructure of the as-cast alloys consisted of austenite phase. As loading, the $\gamma \rightarrow \epsilon$ martensite transformation occurs and is accompanied by obvious work-hardening behaviour. A low SFE and high ΔS_{mix} improved the storage capacity of the dislocation density, promoted the formation of ϵ -martensite, and improve the strength and plasticity. Both the SFE and ΔS_{mix} increased with an increase in the Mn content, and the dislocation density initially increased and then decreased. Optimising the Mn content and coordinating the balance between the SFE and ΔS_{mix} can regulate the optimal dislocation density.

© 2022 The Author(s). Published by Elsevier Ltd. This is an open access article under the CC BY-NC-ND license (http://creativecommons.org/licenses/by-nc-nd/4.0/).

E-mail addresses: zhaoyanchun@lut.edu.cn (Y. Zhao), liws@lut.edu.cn (W. Li), pliaw@utk.edu (P.K. Liaw).

^{*} Corresponding authors.

1. Introduction

Medium- and high entropy alloys (MEAs and HEAs) have attracted considerable attention owing to their excellent mechanical properties and unique deformation mechanisms [1]. In contrast to the design concept of traditional alloys, high-entropy alloys are typically comprised of four or more principal elements, and their atomic percentage (at.%) of each element is 5 %-35 %[2-5]. The higher mixing entropy inhibits the formation of intermetallic compounds and helps the HEA to form simple solid-solution phases [6]. The design strategy of HEAs provides possibilities for obtain promising properties, such as outstanding fracture toughness at cryogenic temperatures, high-temperature softening resistance, strength and ductility synergy, and special magnetic properties [7-12]. HEAs undergo different stages of development. Early HEAs composed of five main elements in equimolar ratios are called the first generation of HEAs, such as CoCrFeNiMn [13], AlCoCrFeNiTi [14], and GdHoLaTbY [15]. Second-generation HEAs, such as FeCoNiCrTi_{0,2} [16], Fe₄₀Mn₂₀Cr₂₀Ni₂₀ [17], and Fe₄₂Mn₃₈-Co₁₀Cr₁₀ [18] exhibit unequal atomic ratios. They mainly perform composition regulation and microstructure optimisation based on first-generation studies, such as introducing dislocations for strengthening [19], increasing the dislocation density to improve fracture toughness [20], and phase change to improve the strength of the alloy [21].

The strengthening mechanism of the phase transformationinduced plasticity (TRIP) effect in MEAs and HEAs has been studied extensively [22-24]. Wei [25] found that the stacking fault energy (SFE) can be reduced by increasing the Co content in the FeMn-CoCrNi alloy, which causes the deformation mechanism of the FeMnCoCrNi alloy to change from dislocation slip to martensiticphase transformation, thus realising the optimisation of mechanical properties. Chen [26] investigated the synergistic effects among the local chemical composition, TRIP effect, and microstructural evolution of high-entropy alloys. The results indicated that the interactions between dislocations and stacking faults promoted the formation of hexagonal close packed (HCP) structures, which led to a change in the local chemical composition of the alloy, promoted the formation of the Lomer-Cottrell dislocation lock, hindered dislocation movement, and improved the work-hardening rate of the alloy. The TRIP effect was first proposed in the study of high-manganese steels, where Fe and Mn are essential. Mn plays an important role in realising the TRIP effect by adjusting the phase stability to activate dislocation transformation. Li [27,28] designed a phase-transformation-induced plasticity Fe_{80-x}Mn_xCo₁₀Cr₁₀ high entropy alloy (TRIP-HEA) with a dual-phase structure (FCC + HCP) by adjusting the content of alloy element, Mn, to regulate the SFE. The deformation mechanisms of transformation, stacking fault, and dislocation slips were combined to realise simultaneous improvement of both the strength and plasticity. It is worth mentioning that dislocations are the main source of strength in most metal structural materials [29,30]. However, when the dislocation density is sufficiently high, it is difficult to obtain a numerical value by traditional transmission electron microscopy (TEM) observations, which introduces difficulties and controversies to the quantitative characterisation of the contribution of dislocation strengthening and even the qualitative judgment of the main strengthening modes of materials [31,32]. Therefore, it is vital to analyse the diffraction peak broadening and cooperate with the corresponding theoretical model. For example, the modified Warren-Averbach method can relate the different diffraction peaks to the dislocation density of the material.

In this study, the effects of Mn on the microstructure and mechanical properties of Fe-XMn-5Si-10Cr-0.9C (X = 10, 15, 20,

and 25 wt%) MEAs were investigated. Thermodynamic models for calculating the SFE and semi-quantitative calculation of the alloy dislocation density were used to analyse the deformation behaviour, and the work-hardening and strengthening mechanisms were discussed.

2. Materials and methods

Ingots of Fe-XMn-5Si-10Cr-0.9C (X = 10, 15, 20, and 25 wt%) MEAs, labelled as 10Mn, 15Mn, 20Mn, and 25Mn, were prepared by magnetic suspension melting in a water-cooled copper crucible, and casted in a negative pressure suction casted copper mould. Raw Fe, Mn, Si, Cr, and C with purities higher than 99.9 wt% were used. All ingots were melted three times to ensure the compositional homogeneity. The phase structure was investigated via Xray diffraction (XRD) analysis using an EMPYREAN with the Cu Kα radiation in the 2θ range of 30° to 100°. And the crystal structures refining was performed by using the Full-Prof software program (Rietveld analysis). The fracture morphology of the alloy after compression fracture was observed, employing a OUANTA-FEG450 thermal field-emission scanning electron microscope (SEM). Phase analysis and microstructure characterization of the alloy were performed, using a JEM-2010 transmission electron microscope (TEM). The compression test was conducted at room temperature using a WD-100D micro-control electronic universal testing machine with a loading rate of 0.05 mm/min. Three identical samples were prepared and measured for the compression test. The error of the measured yield strength is within \pm 5 MPa.

3. Results and discussion

3.1. Stacking fault energies of Fe-XMn-5Si-10Cr-0.9C MEAs

The thermodynamic parameters of the Fe-XMn-5Si-10Cr-0.9C (X = 10, 15, 20, and 25 wt%) alloy are shown in Fig. 1. From Equation (1), the mixed entropy values range from 1.14 to 1.31R, indicating that their ΔS_{mix} value is within the medium entropy criterion area (1R $\leq \Delta S_{mix} <$ 1.5R). From Equation (2), the mixing enthalpy varies between - 20.67 to - 19.61 kJ/mol. The addition of Mn promoted a negative mixing enthalpy in the alloy, while the entropy gradually increased. Thus, the phase-transformation driving force of the solid–liquid transformation increased, which is conducive to improve the phase stability.

$$\Delta S_{mix} = -R \sum_{i=1}^{i} x_i ln x_i \tag{1}$$

Here, R is the gas constant, $8.314 \text{ J/(mol} \bullet \text{K)}$, and x_i denotes the atomic content of the i^{th} principal component.

$$\Delta H_{mix} = \sum_{i=1, i \neq j}^{N} 4\Delta H_{ij}^{mix} x_i x_j \tag{2}$$

Here, x_i and x_j denote the mixing enthalpies of binary liquid alloys with atomic percentages of i and j in regular melts, respectively.

The modified Olsen–Cohen thermodynamic model was used to calculate the SFE of the alloy. The calculation formula for SFE is shown in Equation (3) [33]:

$$SFE = 2\rho\Delta G^{\gamma \to \varepsilon} + 2\sigma^{\gamma \to \varepsilon} \tag{3}$$

where ρ denotes the molar surface density along the {111} planes, $\rho = 4/(\sqrt{3} \ a^2 N)$. N is Avogadro's constant and the lattice parameter is taken as a = 0.36 nm. $\sigma^{\gamma \to \epsilon}$ denotes the interfacial energy between the γ and ϵ phases, which is taken as 10 mJ/m²,

Y. Zhao, H. Ma, L. Zhang et al. Materials & Design 223 (2022) 111241

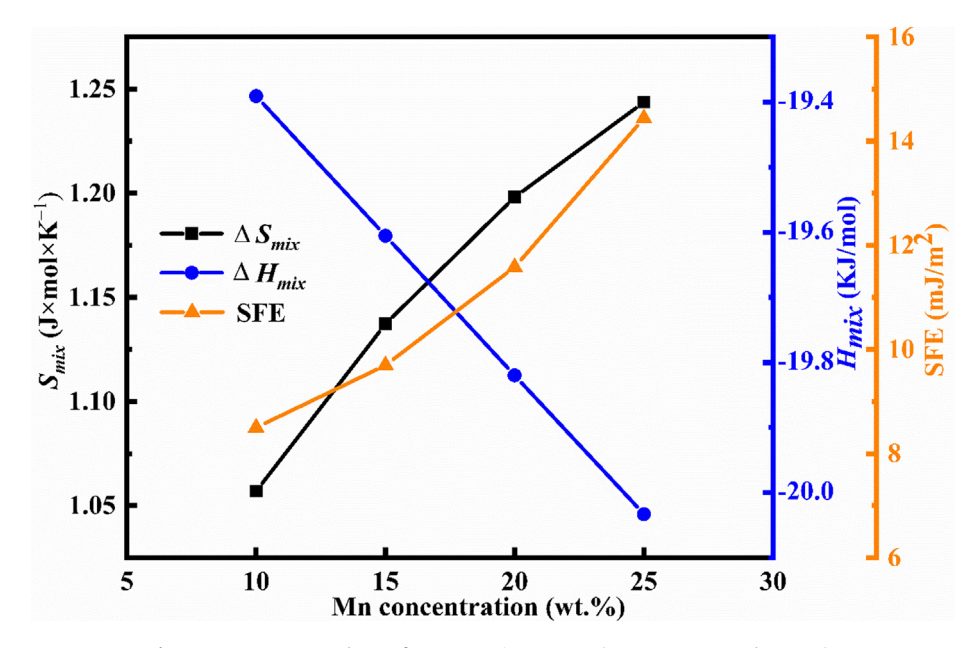


Fig. 1. ΔS_{mix} , ΔH_{mix} , and SFE of Fe-XMn-5Si-10Cr-0.9C (X = 10, 15, 20, and 25 wt%).

and $\Delta G^{\gamma \to \epsilon}$ denotes the Gibbs free energy difference during the transformation from γ -austenite to ϵ -martensite, which can be expressed by the following equation [34,35]:

$$\begin{split} \Delta G^{\gamma \to \epsilon} &= X_{Fe} \Delta G_{Fe}^{\gamma \to \epsilon} + X_{Mn} \Delta G_{Mn}^{\gamma \to \epsilon} + X_{Si} \Delta G_{Si}^{\gamma \to \epsilon} + X_{Cr} \Delta G_{Cr}^{\gamma \to \epsilon} \\ &+ X_C \Delta G_C^{\gamma \to \epsilon} + X_{Fe} X_{Mn} \Delta \Omega_{FeMn}^{\gamma \to \epsilon} + X_{Fe} X_{Si} \Delta \Omega_{FeSi}^{\gamma \to \epsilon} \\ &+ X_{Fe} X_{Cr} \Delta \Omega_{FeCr}^{\gamma \to \epsilon} + X_{Fe} X_C + \Delta G_{mg}^{\gamma \to \epsilon} \end{split} \tag{4}$$

From Fig. 1, the value of the SFE is between $\sim 8.50\text{--}14.44~\text{mJ/m}^2$. The SFE decreased with a decrease in the Mn content. A low stacking fault energy increased the plane-slip degree of dislocations, reduced the cross-slip tendency and annihilation distance of dislocations, and realised the high-density dislocation storage. With a decrease in Mn, ΔS_{mix} also decreased, which reduced the lattice distortion and the high entropy effect, restricting the dislocation storage capacity. Thus, optimising the Mn content and coordinating the competition between SFE and ΔS_{mix} can regulate the optimal dislocation density.

3.2. Phase analyses and microstructure characterization

The XRD patterns of the as-cast Fe-XMn-5Si-10Cr-0.9C (X = 10, 15, 20, and 25 wt%) alloys are shown in Fig. 2(a). Meanwhile, the Rietveld refined results and the quantity of the relevant diffraction peaks are manifested in Fig. 2 (b) and (c), respectively. With an increase in the Mn content, the position of the diffraction peak does not change and is mainly composed of the austenite phase. The addition of Mn enlarged the austenite-phase region and increased the stability of supercooled austenite. Fig. 3(a) shows the XRD patterns of the fractured samples of the Fe-XMn-5Si-10Cr-0.9C (X = 10, 15, 20, and 25 wt%) alloys. A part of the austenite was induced during the martensite transformation with loading. With the increase of Mn content, the amount of epsiron martensite increased first then decreased. From Fig. 3(b) and (c), with the increase of Mn content, the amount of epsiron martensite from the fractured samples after loading, increased first and then decreased, and X = 15 is the highest among them, indicating that more \(\varepsilon\)-martensite were induced with loading [36]. Firstly, from Fig. 1, both the SFE and ΔS_{mix} increases with the increase of the Mn content. However, they play opposite roles in the martensitic transformation. Low SFE and high ΔS_{mix} improve the storage capacity of the dislocation density, promote the formation of ϵ -martensites. The lower stacking fault energy increases the planar-slip degree of dislocations, reduces the annihilation distance of dislocations, and improves the high-density dislocation storage. The higher ΔS_{mix} promotes the lattice distortion and enhances the dislocation storage capacity. Thus, optimizing the Mn content and coordinating the competition between the SFE and ΔS_{mix} , can regulate the optimal dislocation density.

Fig. 4a shows the microstructure and dislocation distribution of the as-cast 15Mn. The alloy solidified under a higher cooling rate condition (cooling rate below 10³ K/s), forming supersaturated vacancies, which aggregated to form dislocations. From Fig. 4(b), HRTEM images and the corresponding fast Fourier transform (FFT) patterns analyses, a large amount of edge dislocations in the as-cast alloy are observed. From the bright-field image in Fig. 4 (c), dense dislocations are accumulated in the martensite laths after loading, which hinders the dislocation slip and improves the strength of the alloy. The SAED patterns in Fig. 4 (c) and the corresponding dark-field TEM images in Fig. 4 (d), exhibit the retained austenite matrix (Point 1), the ε-martensite lath (Point 2), and their dislocations distribution. Moreover, as shown in Fig. 4e, several stacking faults could be found in the amplified remaining austenite matrix, indicating that stacking-fault nucleation occurred and may have promoted the ε-martensite transformation [37].

Fig. 5 shows the metallographic as-cast structure from the edge to the centre of the sample. Owing to the rapid heat transfer between the melt and the copper mould during solidification, a fine grain edge and equiaxed centre were observed. Owing to the thermal stress and preferred orientation grain growth under the temperature gradient, the extrusion of adjacent grains led to a decrease in grain uniformity, resulting in as-cast dislocations. Moreover, MEAs have several components, and large atomic radius differences led to a high lattice distortion, resulting in better fine-grain effects and even lattice collapses to induce a high dislocation density and dense boundary.

Fig. 6(a) shows the energy dispersive X-ray spectroscopy (EDS) elemental surface distribution of the as-cast alloy structure using TEM observations. The results indicated that Fe, Mn, Si, and C were

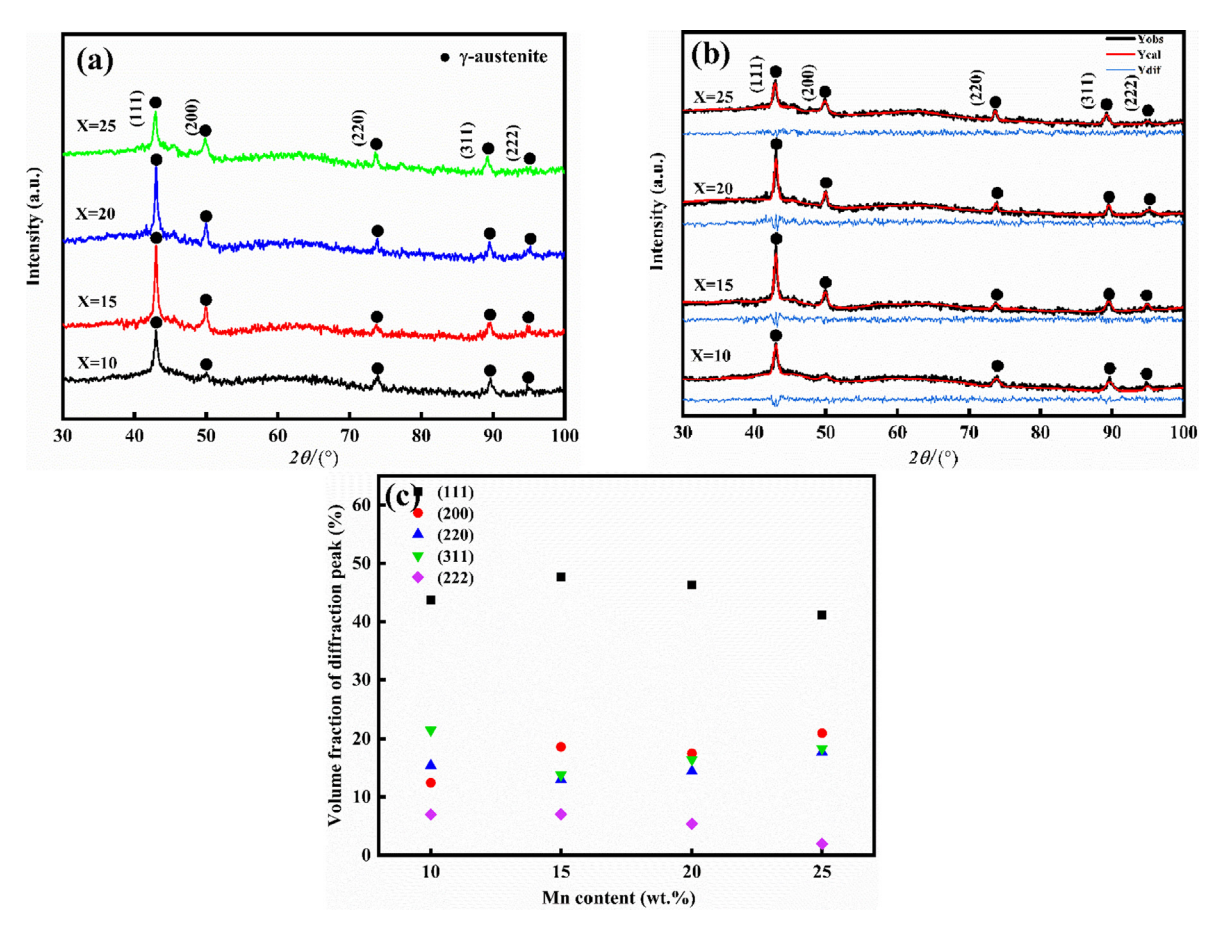


Fig. 2. (a) XRD curves, (b) Rietveld refinements of the spectrum, (c) Volume fraction of different peaks of Fe-XMn-5Si-10Cr-0.9C (X = 10 ~ 25, wt.%) as-cast samples.

uniformly distributed in the as-cast alloy. From Fig. 6(b), the high-angle annular dark-field scanning transmission electron microscopy (HADDF-STEM), the distributions of Fe, Mn, Si, Cr, and C were uniform, and no micro segregation was found, indicating that the MEA was composed of a solid-solution phase with a single and uniform structure.

3.3. Dislocation densities of Fe-XMn-5Si-10Cr-0.9C MEAs

The dislocation density of the alloy specimens could be calculated using the XRD data combined with the modified Warren-Averbach (W-A) or Willianson-Hall (W-H) equations [38-41]. The full width at half maximum (FWHM) of each diffraction peak of the as-cast sample (Fig. 1) ((111), (200), (220), (311), and (222)) was calculated using JADE software and was shown in Fig. 7. As the Mn content increases, FWHM of (111) increases first and then decreases, and those of x = 25 were the lowest, which indicate that the dislocation density changed correspondingly. However, FWHM of x = 15 are the highest except for (222), which is attributed to the anisotropic broadening of the diffraction profile. Because the dislocations can not be completely symmetrical to the diffraction vector, the diffraction profiles exhibit anisotropic broadening. From Fig. 2 (c) and Fig. 3 (c), after loading, the volume fraction of (111) obviously decreases, and other diffraction peaks have no significant changes. As mentioned in Fig. 1, the Fe-XMn-5Si-10Cr-0.9C alloys possesses the lower SFE (8.50 \sim 14.44 mJ/m ²), which is conducive to decompose the 1/2 < 110 > total dislocation of the $\{111\}$ γ plane into two 1/6 < 112 > Shockley incomplete dislocations. Therefore, as the main diffraction peak, (111) plays the primary role in the calculation of the total dislocation density and martensitic transformation volume.

As MEAs undergo martensitic transformation after loading, the dislocation configuration changes during deformation, and the $R_{\rm e}$ value should be considered when calculating the dislocation density. $R_{\rm e}$ is the effective outer radius of dislocation distribution. However, $R_{\rm e}$ is only reflected in the "tail" of the diffraction peak. The modified W-A method is based on the discrete Fourier transform of the diffraction peak, taking into account the peak tail information and $R_{\rm e}$, whereas the FWHM used in the modified W-H method ignores the additional information of the tail of the diffraction peak [42]. Thus, we used the modified W-A equation to calculate the dislocation density. The W-A equation is shown in Equation (5) [43]:

$$\ln A(L) \cong \ln A^{S}(L) - \rho B L^{2} \ln \frac{R_{e}}{L} (K^{2} \bar{C}) + O(K^{4} \bar{C}^{2})$$
 (5)

where A(L) denotes the true part of the Fourier coefficient. L denotes the Fourier length, L = na_3 , n is a positive number starting from zero, $a_3 = \lambda/2(sin\theta_2 - sin\theta_1)$, and $\theta_2 - \theta_1$ denotes the angular range of the corresponding measured diffraction surface [44]. B is a constant related to the elastic modulus and dislocation configuration of the material, and $O\left(K^4\bar{C}^2\right)$ is a high-order term that can be ignored. The Superscript, S, in the first term, the size parameter corresponding to the Fourier coefficients, is denoted by L₀. It is obtained from the size Fourier coefficients, AS, by taking the intercept of the initial slope at AS = 0. The Fourier coefficient, A(L), was obtained by the Fourier analysis of the diffraction peaks [45–47]. The dislocation density can be determined from the coefficient of

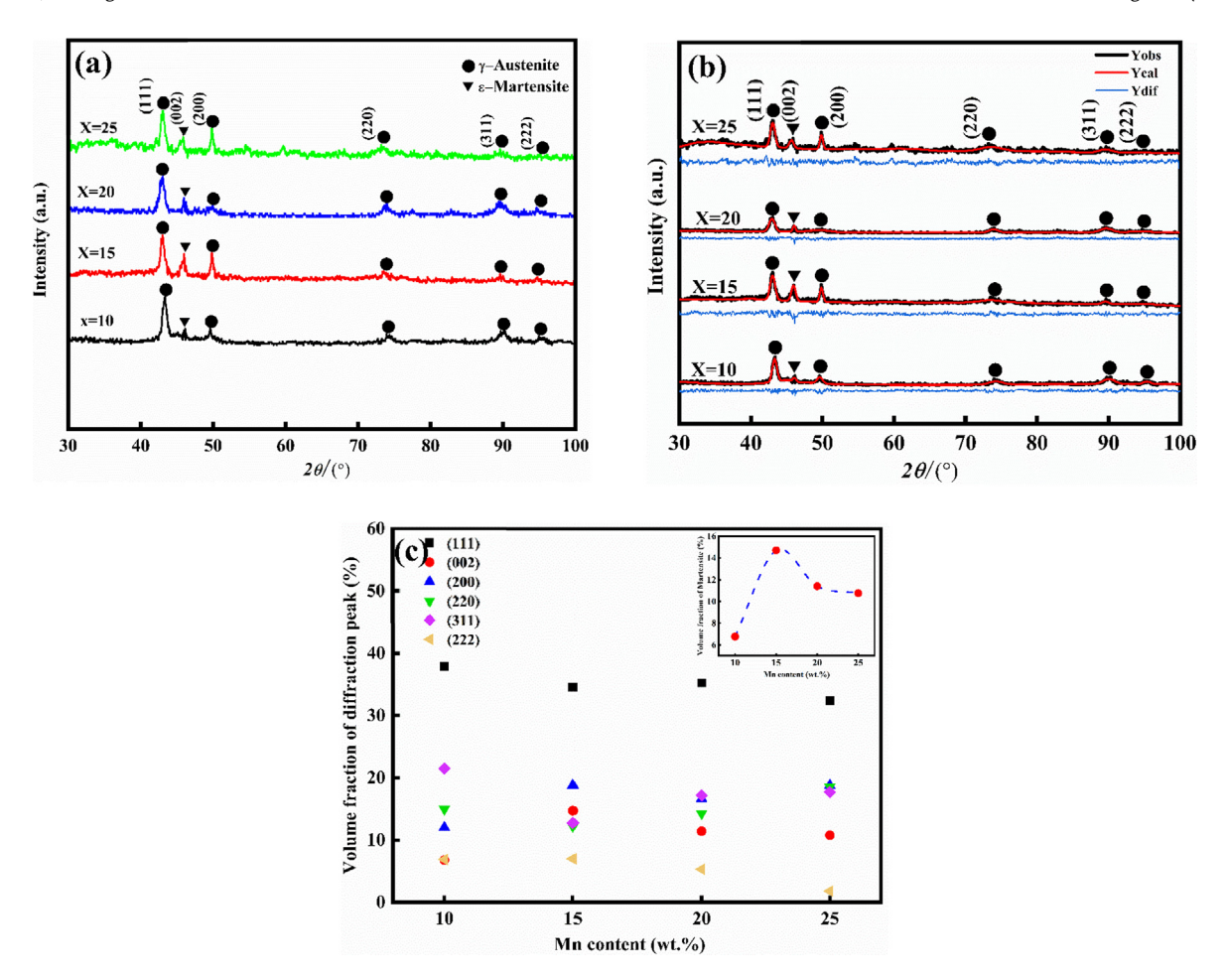


Fig. 3. (a) XRD curves, (b) Rietveld refinements of spectrum, (c) Volume fraction of different peaks of Fe-XMn-5Si-10Cr-0.9C (X = 10, 15, 20, and 25 wt%) fractured samples.

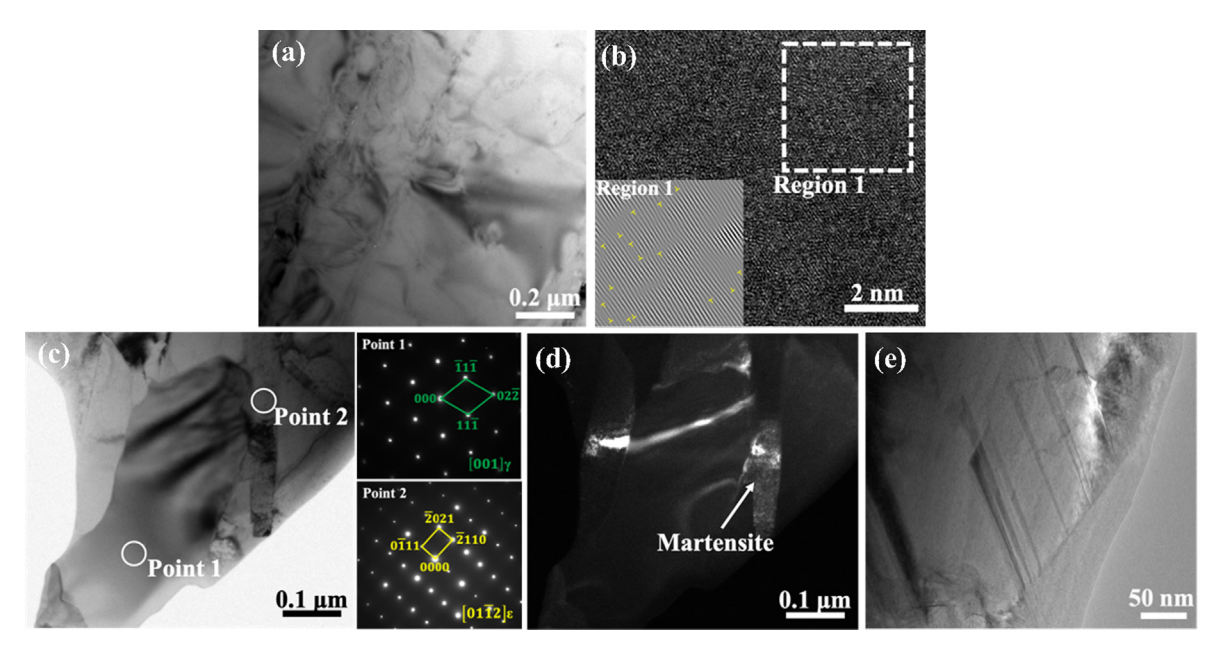


Fig. 4. (a) TEM image, (b) HRTEM and FFT images of the as-cast alloy, (c) fractured samples and SEAD patterns, (d) dark-field image, (e) stacking faults in the remaining austenite matrix of the Fe-15Mn-5Si-10Cr-0.9C alloy.

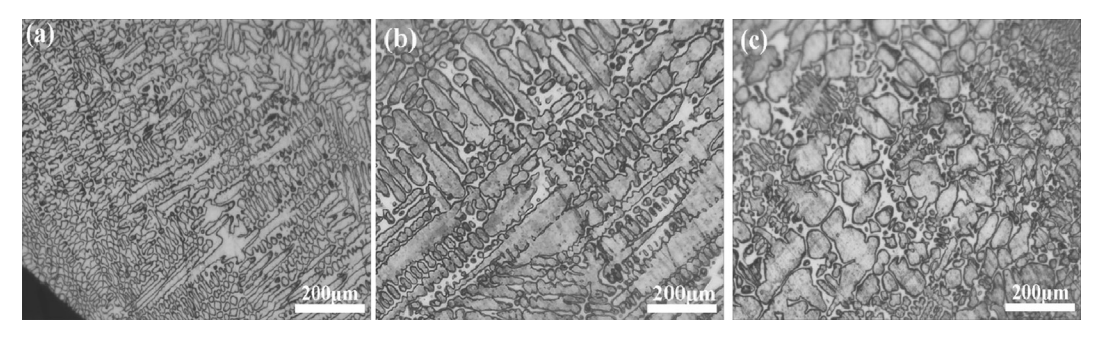
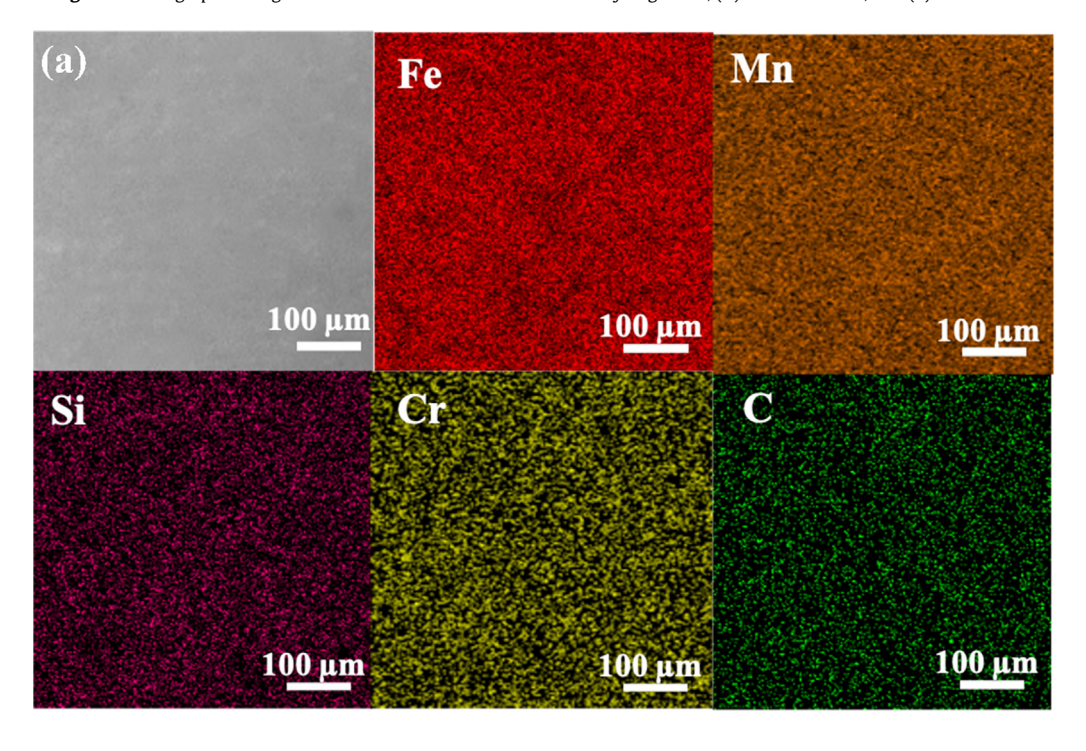


Fig. 5. Metallographic images of Fe-15Mn-5Si-10Cr-0.9C as-cast alloy Edge area, (b) transition area, and (c) central area.



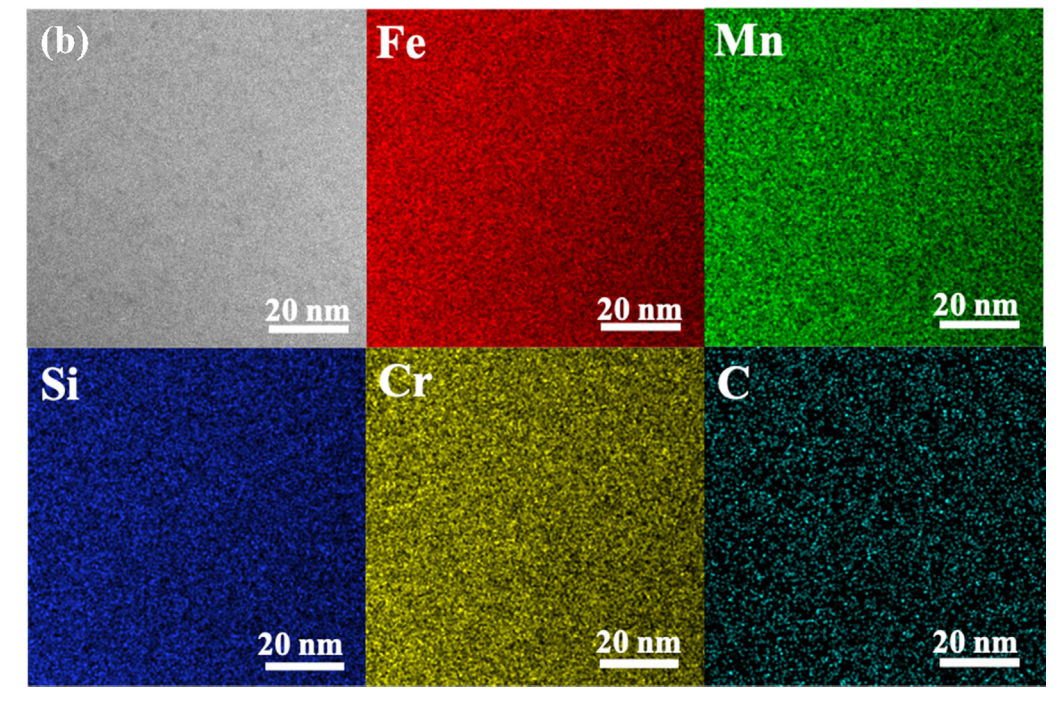


Fig. 6. (a) EDS elemental distribution maps, (b) HAADF-STEM images of Fe-15Mn-5Si-10Cr-0.9C as-cast alloy.

Y. Zhao, H. Ma, L. Zhang et al.

Materials & Design 223 (2022) 111241

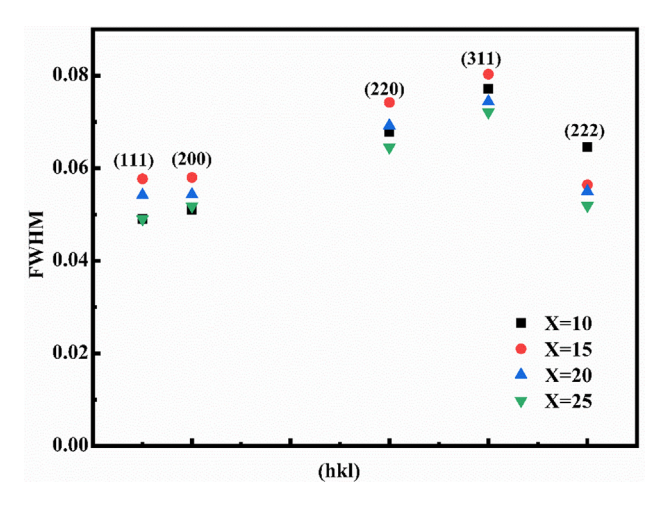


Fig. 7. FWHM of diffraction peaks in Fe-XMn-5Si-10Cr-0.9C as-cast alloys.

the second term in Equation (5). Thus, the Fourier coefficients shown in Fig. 8 show obviously different tendencies among samples with different Mn contents, indicating the dislocation density changes correspondingly.

Using Equation (5), it is evident that $\ln A(L)$ has a linear relationship with K^2 \bar{C} . It can be observed from Fig. 8, that when the Fourier length, L, is given, there is a corresponding A(L), which is the true

part of the Fourier coefficient. Linear fitting was performed on $\ln A(L)$ and $K^2 \bar{C}$, and a W-A diagram of MEAs with different Mn contents was obtained, as shown in Fig. 9 [47].

The slope associated with each L coefficient, which is the true coefficient of $K^2 \bar{C}$ in Equation (5), can be obtained from Fig. 10. It is necessary to set this coefficient as Y to obtain an equation for Y, as shown in Equation (6) [48].

$$Y = \rho \frac{\pi b^2}{2} L^2 ln \frac{R_e}{L} \tag{6}$$

$$\frac{Y}{L^2} = \rho \frac{\pi b^2}{2} lnR_e - \rho \frac{\pi b^2}{2} lnL \tag{7}$$

Thus, Y denotes the slope of each straight line obtained from Fig. 10, which varies with L. ρ denotes the required dislocation density, R_e the effective circumscribed radius, b the Bergs vector, and b = 0.254 nm [49]. Equation (7) can be obtained from Equation (6). Y/L² had a linear relationship with lnL. Based on the results in Fig. 9, linear fitting was performed on Y/L² - lnL, and the relationship curve diagram of Y/L² - lnL was obtained, as shown in Fig. 10.

The slope of each curve is – $\rho(\pi b^2/2)$, which increased first and then decrease, indicating that the dislocation density undergoes obvious changes as Mn content increases. Hence, the slopes are – 2.3×10^{-4} , – 4.9×10^{-4} , – 3.02×10^{-4} and – 2.56×10^{-4} , respectively. It can be determined that the dislocation density of the FeXMn-5Si-10Cr-0.9C (X = 10, 15, 20, and 25 wt%) alloys are

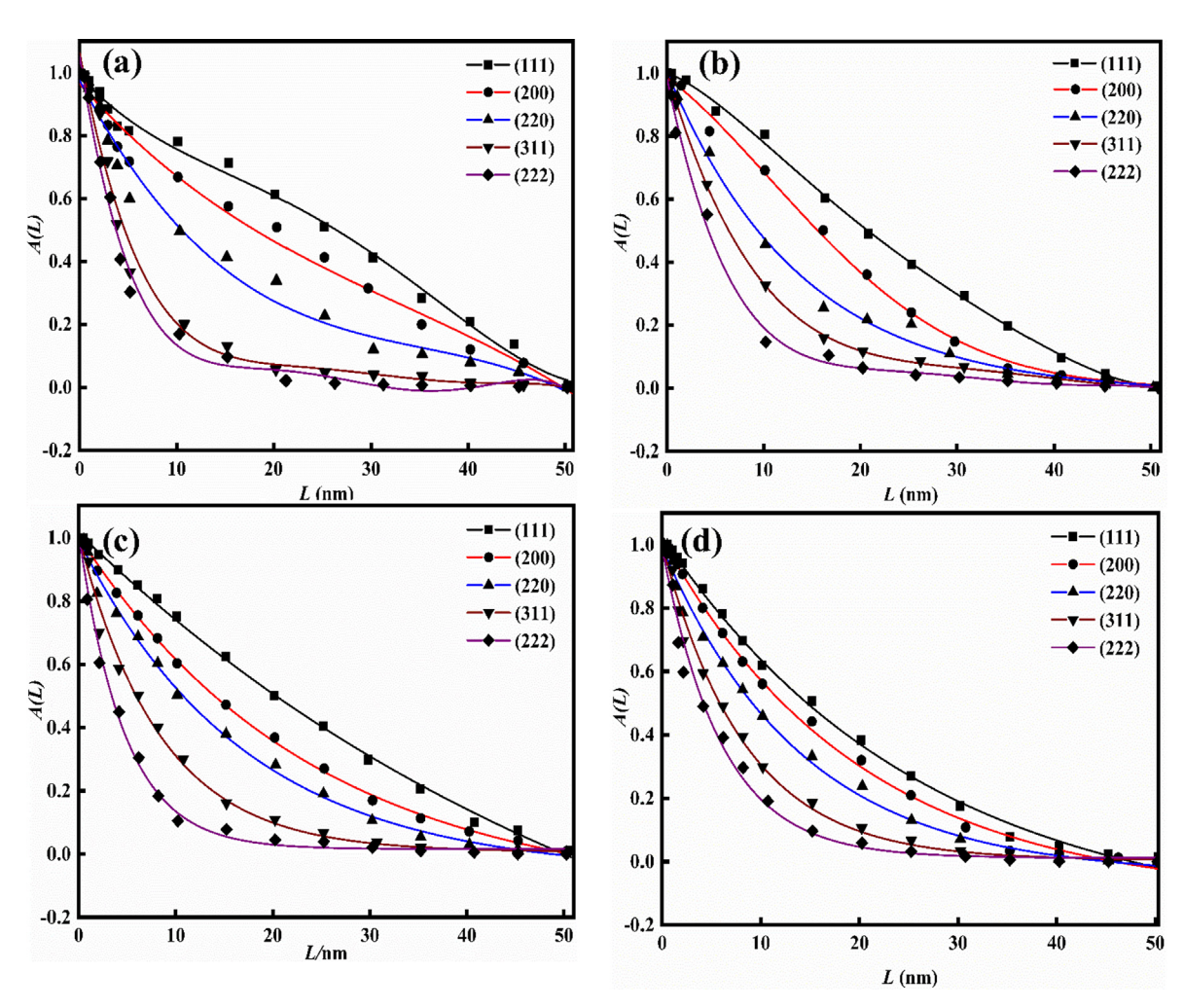


Fig. 8. Fourier coefficients of the Fe-XMn-5Si-10Cr-0.9C as-cast alloys (a) for X = 10 (b) for X = 15 (c) for X = 20 (d) for X = 25.

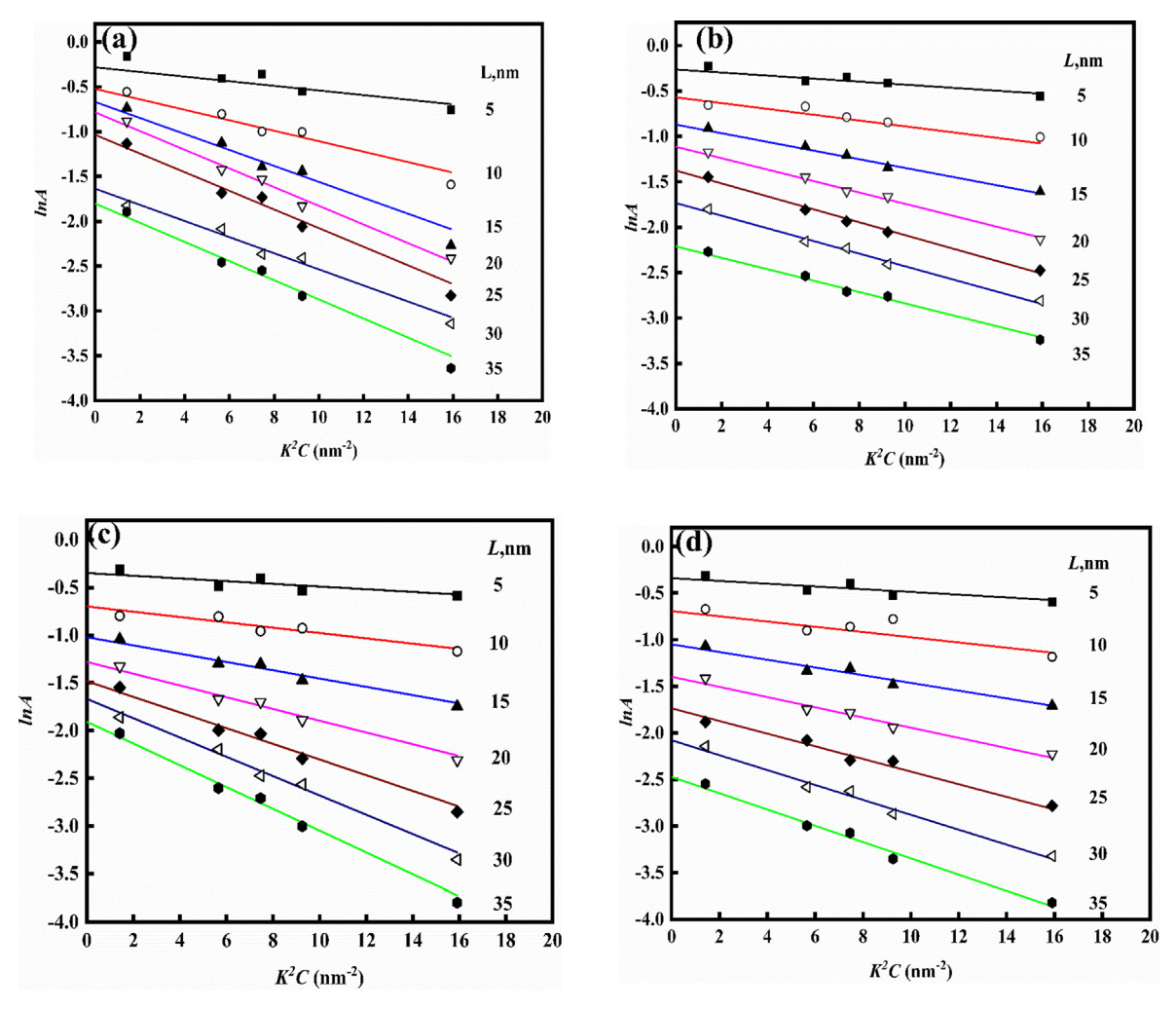


Fig. 9. W-A diagrams of the Fe-XMn-5Si-10Cr-0.9C as-cast alloys (a) for X = 10 (b) for X = 15 (c) for X = 20 (d) for X = 25.

 2.3×10^{15} , 4.8×10^{15} , 3×10^{15} , and 2.5×10^{15} m $^{-2}$, respectively. The dislocation density of the MEAs was significantly higher than that of the general cast alloy. As mentioned, the uneven heat dissipation of crystallisation cooling and the different cooling coefficients between the alloy melt and the copper crucible produced thermal stresses in the ingot, which led to dislocation defects. Second, the temperature gradient and magnetic stirring during the melting process affected crystal growth, and the adjacent grains deflected or bent to form a phase difference, resulting in dislocations. Moreover, the alloy had a lower SFE, which is conducive to the dislocation planar slip, reducing the dislocation cross-slip tendency and annihilation distance, and realising the storage of a higher dislocation density.

3.4. Compressive properties

Fig. 11 shows the quasi-static compressive stress-strain curves of different Mn contents. Table 1 gives the compressive yield strength, fracture strength and plastic strain, respectively. The yield strength of the alloy increased with increasing Mn content, whereas the fracture strength and plastic strain initially increased and then decreased. When the Mn content was 15 wt%, the alloy had better comprehensive mechanical properties. Compared with the 20Mn alloy, its fracture strength increased by 0.8 %, and the plastic strain was 5 % higher than that of the 10Mn alloy. As men-

tioned, the stress induces martensitic transformation with loading, and dislocations accumulate in the martensite laths. Thus, dislocation slip was blocked, which improved the strength of the alloy. Moreover, the formation of martensite causes volume expansion, leading to the introduction of high-density dislocations. Immovable dislocations, formed by mutual entanglement between dislocations, play a strengthening role. The 15Mn alloy with a lower SFE is conducive to decomposing the $1/2 \ \langle 110 \rangle$ total dislocation of the $\{111\}\gamma$ plane into two $1/6 \ \langle 112 \rangle$ Shockley incomplete dislocations. The expansion of stacking faults provided a nucleation core for the $\gamma \to \epsilon$ phase transition and promoted the formation of the ϵ -martensite. In addition, the high dislocation density in the 15Mn alloy improved the strength of the alloy.

The corresponding work-hardening curves are shown in Fig. 12. With an increase in true strain, the work-hardening rate can be divided into three stages. In the first stage, owing to the sharp increase in the dislocation density, the work-hardening rate is high. However, with the start of the slip system and the recovery of a large number of dislocations, the work-hardening rate begins to decrease sharply. Early in the second stage, the 15Mn alloy entered the platform stage before the other alloys. With an increase in strain, the work-hardening rate of the 15Mn alloy was higher than that of the other alloys. During the third stage, the work-hardening rate decreased continuously before the fracture stage. Because the martensite produced was close to saturation, the rate of dislocation multiplication was reduced, resulting

Y. Zhao, H. Ma, L. Zhang et al.

Materials & Design 223 (2022) 111241

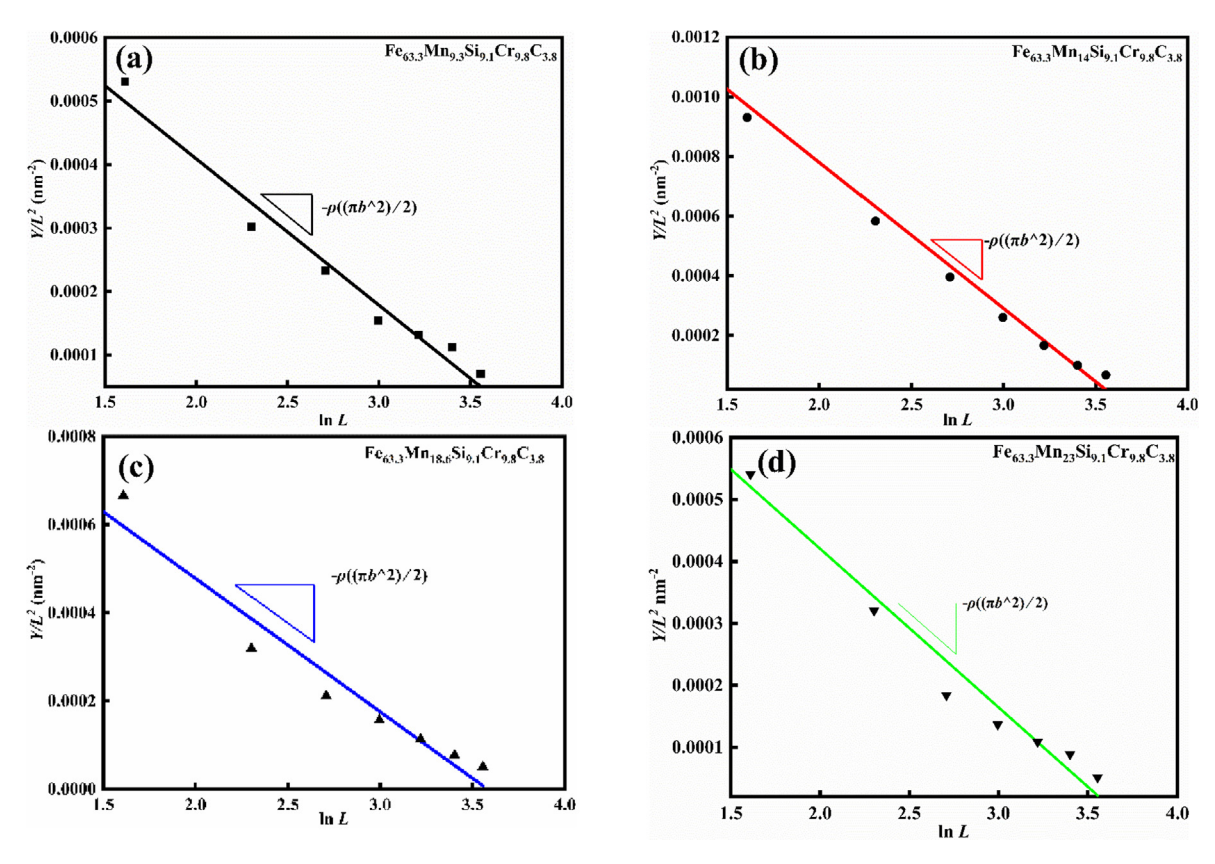


Fig. 10. Y/L² - InL relationship diagrams of the Fe-XMn-5Si-10Cr-0.9C as-cast alloys (a) for X = 10 (b) for X = 15 (c) for X = 20 (d) for X = 25.

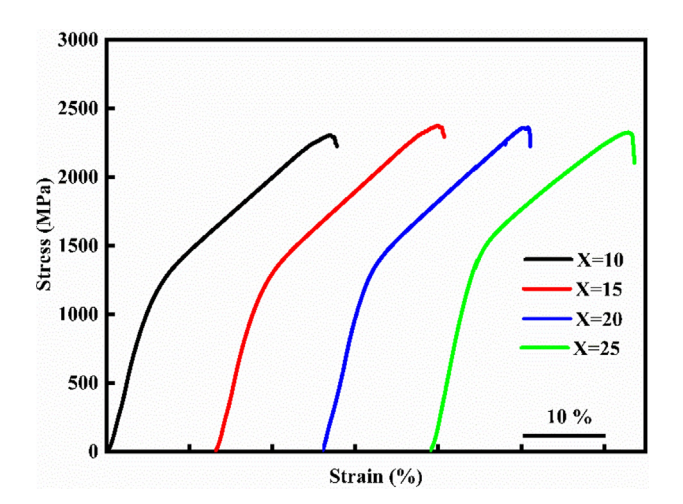


Fig. 11. Engineering stress–strain curves of Fe-XMn-5Si-10Cr-0.9C (X = 10, 15, 20,and 25 wt%) alloys.

Table 1 Compressive properties of Fe-XMn-5Si-10Cr-0.9C (X = 10, 15, 20, and 25 wt%) alloys (σ_s : yield strength; σ_f : fracture strength; ϵ_p : plastic strain).

Samples	$\sigma_{\rm f} (\text{MPa})$	ε _p (%)	σ_s (MPa)
Fe-10Mn-5Si-10Cr-0.9C	2,306	15.9	1,250
Fe-15Mn-5Si-10Cr-0.9C	2,381	16.8	1,266
Fe-20Mn-5Si-10Cr-0.9C	2,361	15.1	1,361
Fe-25Mn-5Si-10Cr-0.9C	2,325	14.7	1,503

in a decrease in the work-hardening rate. Using the Hollomon equation [46], $ln\sigma = lnK + nln\epsilon$, we could obtain the average work-hardening index, n, of the alloys. The n values of the Fe-

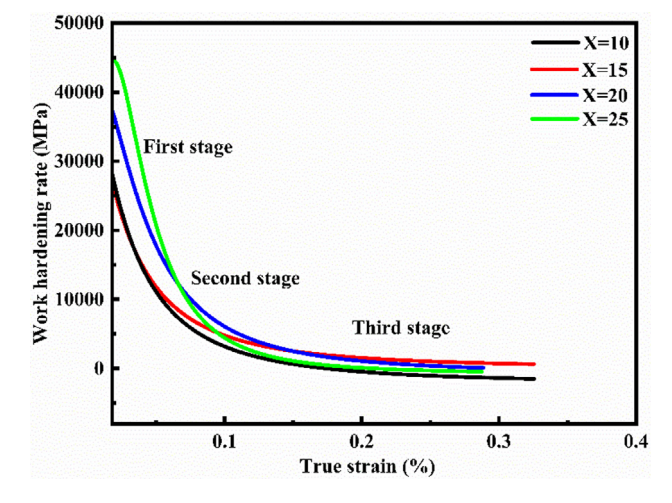


Fig. 12. The relationship between the work-hardening rate and true strain of Fe-XMn-5Si-10Cr-0.9C (X = 10, 15, 20, and 25 wt%) alloys.

XMn-5Si-10Cr-0.9C (X = 10, 15, 20, and 25 wt%) alloys were determined to be 0.36, 0.42, 0.37, and 0.34, respectively. The work-hardening index of the alloys was high, and when the Mn content was 15 wt%, the work-hardening ability of the alloy peaked.

Fig. 13 shows the fracture morphologies of the MEAs. Both the 10Mn and 15Mn alloys have dense and deep dimples and some tearing edges present close to the cross-section. The number of dimples decreased significantly, accompanied by fluvial patterns, in the 20Mn and 25Mn alloys. During deformation, dislocations multiply and accumulate at the phase boundary, resulting in stress concentration, microcrack nucleation, and rapid propagation, and eventually leading to fracture failure.

Y. Zhao, H. Ma, L. Zhang et al.

Materials & Design 223 (2022) 111241

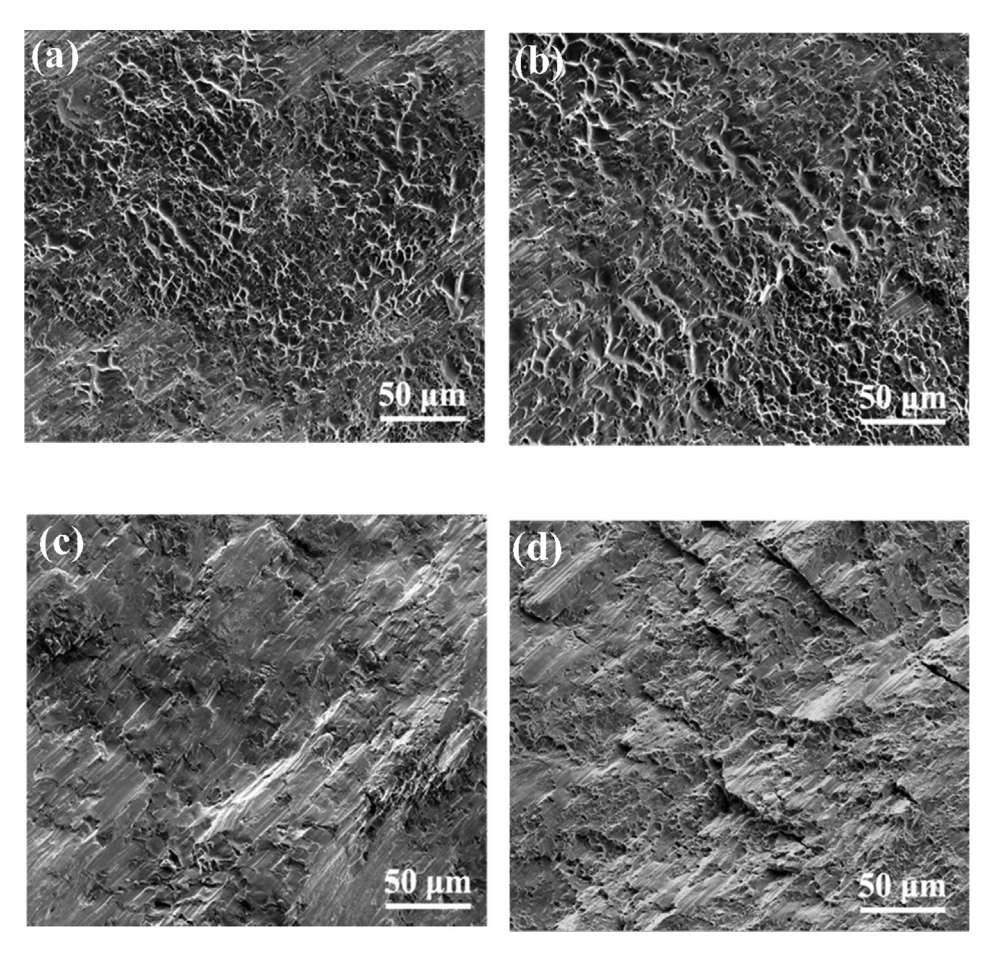


Fig. 13. Fracture morphologies of Fe-XMn-5Si-10Cr-0.9C (X = 10, 15, 20, and 25 wt%) alloys 10Mn, (b) 15Mn, (c) 20Mn, and (d) 25Mn.

4. Conclusions

In this study, the effects of Mn content on the microstructures, stacking fault energy, dislocation density, and mechanical properties of the Fe-XMn-5Si-10Cr-0.9C (X = 10, 15, 20, and 25 wt%) MEAs were investigated. The main conclusions are described as follows:

- (1) The SFE of the Fe-XMn-5Si-10Cr-0.9C MEAs is between ~ 8 . 50–14.44 mJ/m², which improves the storage capacity of the dislocation density, promotes the formation of ϵ -martensites, and improves the strength and plasticity.
- (2) MEAs possess a uniquely high dislocation density. The dislocation density increased initially and then decreased with increasing Mn content, up to $4.8\times10^{15}~\text{m}^{-2}$ when the Mn content is 15 wt%.
- (3) As the Mn content increased from 10 to 25 wt%, the yield strengths of the alloys increased substantially from 1,250 to 1,503 MPa, whereas the fracture strengths increased initially and then decreased. The Fe-15Mn-5Si-10Cr-0.9C alloy possesses a good work-hardening capacity with fracture and yield strengths of 2,381 and 1,266 MPa, respectively. The outstanding mechanical properties were attributed to dislocation strengthening and phase transformation-induced plasticity (TRIP) effects.

Data availability

Data will be made available on request.

Declaration of Competing Interest

The authors declare that they have no known competing financial interests or personal relationships that could have appeared to influence the work reported in this paper.

Acknowledgements

Yanchun Zhao gratefully acknowledge the fundings by National Natural Science Foundation of China (Grant 52061027), and Hongliu Outstanding Talents Program of Lanzhou University of Technology (Grant 2018). Wensheng Li thanks to the supports of Major Special Projects of Gansu Province (21ZD4WA017). Peter K. Liaw very much appreciates the support of the U.S. Army Research Office Project (W911NF-13-1-0438 and W911NF-19-2-0049) with the program managers, Drs. M. P. Bakas, S. N. Mathaudhu, and D. M. Stepp and the support from the National Science Foundation (DMR-1611180 and 1809640) with the program directors, Drs. J. Yang, G. Shiflet, and D. Farkas.

References

- [1] J.W. Yeh, S.K. Chen, S.J. Lin, J.Y. Gan, T.S. Chin, T.T. Shun, C.H. Tsau, S.Y. Chang, Nanostructured high-entropy alloys with multiple principal elements: novel alloy design concepts and outcomes, Adv. Eng. Mater. 6 (2004) 299–303.
- [2] B. Cantor, I.T.H. Chang, P. Knight, A.J.B. Vincent, Microstructural development in equiatomic multicomponent alloys, Mater. Sci. Eng. A 375 (2004) 213–218.
- [3] Y. Zhang, T.T. Zuo, Z. Tang, M.C. Gao, K.A. Dahmen, P.K. Liaw, Z.P. Lu, Microstructures and properties of high-entropy alloys, Prog. Mater. Sci. 61 (2014) 1–93.

- [4] O.N. Senkov, G.B. Wilks, D.B. Miracle, C.P. Chuang, P.K. Liaw, Refractory highentropy alloys, Intermetallics 18 (9) (2010) 1758–1765.
- [5] J.Y. He, W.H. Liu, H. Wang, Y. Wu, X.J. Liu, T.G. Nieh, Z.P. Lu, Effects of Al addition on structural evolution and tensile properties of the FeCoNiCrMn high-entropy alloy system, Acta Mater. 62 (2014) 105–113.
- [6] Z.J. Zhang, M.M. Mao, J.W. Wang, B. Gludovatz, Z. Zhang, S.X. Mao, E.P. George, Q. Yu, R.O. Ritchie, Nanoscale origins of the damage tolerance of the high entropy alloy CrMnFeCoNi, Nat. Commun. 6 (2015) 10143–10148.
- [7] P. Shi, R. Li, Y. Li, Y. Wen, Y. Zhong, W. Ren, Z. Shen, T. Zheng, J. Peng, X. Liang, P. Hu, N. Min, Y. Zhang, Y. Ren, P.K. Liaw, D. Raabe, Y.-D. Wang, Hierarchical crack buffering triples ductility in eutectic herringbone high-entropy alloys, Science 373 (6557) (2021) 912–918.
- [8] Q. Pan, L. Zhang, R. Feng, Q. Lu, K.e. An, A.C. Chuang, J.D. Poplawsky, P.K. Liaw, L. Lu, Gradient cell-structured high-entropy alloy with exceptional strength and ductility, Science 374 (6570) (2021) 984–989.
- [9] J. Moon, E. Tabachnikova, S. Shumilin, T. Hryhorova, Y. Estrin, J. Brechtl, P.K. Liaw, W. Wang, K.A. Dahmen, A. Zargaran, J.W. Bae, H.S. Do, B.J. Lee, H.S. Kim, Deformation behavior of a Co-Cr-Fe-Ni-Mo medium-entropy alloy at extremely low temperatures, Mater. Today 50 (2021) 55–68.
- [10] G.N. Zhang, X. Yang, W. Qi, Y. Li, W. Wang, Y.X. Chen, J.T. Li, L.F. Li, Effect of Co on phase stability and mechanical behavior of Co_xCrFeNiMnAl_{0.3} high entropy alloys with micro/nano hierarchical structure, Mater. Des. (2022) 110442–110452
- [11] J.P. Liu, X.X. Guo, Q.Y. Lin, Z.B. He, X.H. An, L.F. Li, P.K. Liaw, X.Z. Liao, L.P. Yu, J.P. Lin, L. Xie, J.L. Ren, Y. Zhang, Excellent ductility and serration feature of metastable CoCrFeNi high-entropy alloy at extremely low temperatures, Sci. China Mater. 62 (2019) 853–863.
- [12] Y.L. Qia, T.H. Cao, H.X. Zong, Y.K. Wu, L. He, X.D. Ding, F. Jiang, S.B. Jin, G. Sha, J. Sun, Enhancement of strength-ductility balance of heavy Ti and Al alloyed FeCoNiCr high-entropy alloys via boron doping, J. Mater. Sci. Technol. 75 (2021) 154–163.
- [13] S.Y. Chen, W.D. Li, X. Xie, J. Brechtl, B. Chen, P.Z. Li, G.F. Zhao, F.Q. Yang, J.W. Qiao, K.A. Dahmen, P.K. Liaw, Nanoscale serration and creep characteristics of Al_{0.5}CoCrCuFeNi high-entropy alloys, J. Alloys Compd. 752 (2018) 464–475.
- [14] Y.J. Zhou, Y. Zhang, Y.L. Wang, G.L. Chen, Solid solution alloys of AlCoCrFeNiTix with excellent room-temperature mechanical properties, Appl. Phys. Lett. 90 (2007) 253–255.
- [15] Y.J. Zhao, J.W. Qiao, S.G. Ma, M.C. Gao, H.J. Yang, M.W. Chen, Y. Zhang, A hexagonal close-packed high-entropy alloy: The effect of entropy, Mater. Des. 96 (2016) 10–15.
- [16] Y. Tong, D. Chen, B. Han, J. Wang, R. Feng, T. Yang, C. Zhao, Y.L. Zhao, W. Guo, Y. Shimizu, C.T. Liu, P.K. Liaw, K. Inoue, Y. Nagai, A. Hu, J.J. Kai, Outstanding tensile properties of a precipitation-strengthened FeCoNiCrTi_{0.2} high-entropy alloy at room and cryogenic temperatures, Acta Mater. 165 (2019) 228–240.
- [17] Y.Z. Wang, Z.M. Jiao, G.B. Bian, H.J. Yang, H.W. He, Z.H. Wang, P.K. Liaw, J.W. Qiao, Dynamic tension and constitutive model in in Fe₄₀Mn₂₀Cr₂₀Ni₂₀ highentropy alloys with a heterogeneous structure, Mater. Sci. Eng. A 839 (2022) 142887–142898.
- [18] L. Qi, X.D. Huang, A.P. Zhang, H.W. Chen, J.F. Nie, Martensitic transformation induced dislocation walls in Fe₄₂Mn₃₈Co₁₀Cr₁₀ high-entropy alloy, Scr. Mater. 201 (2021) 113929–113935.
- [19] Z.W. Wang, I. Baker, Z.H. Cai, S. Chen, J.D. Poplawsky, W. Guo, The effect of interstitial carbon on the mechanical properties and dislocation substructure evolution in Fe_{40.4}Ni_{11.3}Mn_{34.8}Al_{7.5}Cr₆ high entropy alloys, Acta Mater. 120 (2016) 228–239.
- [20] X.X. Zhang, H. Andrä, S. Harjo, W. Gong, T. Kawasaki, A. Lutz, M. Lahres, Quantifying internal strains, stresses, and dislocation density in additively manufactured AlSi10Mg during loading-unloading-reloading deformation, Mater. Des. 198 (2021) 109339–109347.
- [21] P. Agrawal, S. Gupta, S. Shukla, S.S. Nene, S. Thapliyal, M.P. Toll, R.S. Mishra, Role of Cu addition in enhancing strength-ductility synergy in transforming high entropy alloy, Mater. Des. 215 (2022) 110487–110494.
- [22] H. Shahmir, P. Asghari-Rad, M.S. Mehranpou, F. Forghani, H.S. Kim, M. Nili-Ahmadabadi, Evidence of FCC to HCP and BCC-martensitic transformations in a CoCrFeNiMn high-entropy alloy by severe plastic deformation, Mater. Sci. Eng. A 807 (2021) 140875–140878
- [23] W.J. Lu, C.H. Liebscher, G. Dehm, D. Raabe, Z.M. Li, Bidirectional transformation enables hierarchical nanolaminate dual-phase high-entropy alloys, Adv. Mater. 30 (2018) 1–10.
- [24] S.S. Nene, M. Frank, P. Agrawal, S. Sinha, K. Liu, S. Shukla, R.S. Mishra, B.A. McWilliams, K.C. Cho, Microstructurally flexible high entropy alloys: linkages between alloy design and deformation behavior, Mater. Des. 194 (2020) 108968–108978.

- [25] D.X. Wei, X.Q. Li, J. Jiang, W.C. Heng, Y. Koizumi, W.M. Choi, B.J. Lee, H.S. Kim, H. Kato, A. Chiba, Novel Co-rich high performance twinning-induced plasticity (TWIP) and transformation-induced plasticity (TRIP) high-entropy alloys, Scr. Mater. 165 (2019) 39–43.
- [26] S.J. Chen, H.S. Oh, B. Gludovatz, S.J. Kim, E.S. Park, Z. Zhang, R.O. Ritchie, Q. Yu, Real-time observations of TRIP-induced ultrahigh strain hardening in a dual-phase CrMnFeCoNi high-entropy alloy, Nat. Commun. 11 (2020) 826–833.
 [27] Z. Li, K.G. Pradeep, Y. Deng, D. Raabe, C.C. Tasan, Metastable high-entropy dual-
- [27] Z. Li, K.G. Pradeep, Y. Deng, D. Raabe, C.C. Tasan, Metastable high-entropy dualphase alloys overcome the strength-ductility trade-off, Nature 534 (7606) (2016) 227–230.
- [28] Z.M. Li, C.C. Tasan, K.G. Prandeep, D. Raabe, A TRIP-assisted dual-phase high-entropy alloy: grain size and phase fraction effects on deformation behavior, Acta Mater. 131 (2017) 323–335.
- [29] B.B. He, B. Hu, H.W. Yen, G.J. Cheng, Z.K. Wang, H.W. Luo, M.X. Huang, High dislocation density-induced large ductility in deformed and partitioned steels, Science 357 (6355) (2017) 1029–1032.
- [30] P. Zhou, Z.Y. Liang, R.D. Liu, M.X. Huang, Evolution of dislocations and twins in a strong and ductile nanotwinned steel, Acta Mater. 111 (2016) 96–107.
- [31] Z.Y. Liang, Y.Z. Li, M.X. Huang, The respective hardening contributions of dislocations and twins to the flow stress of a twinning-induced plasticity steel, Scr. Mater. 112 (2016) 28–31.
- [32] I. Gutierrez-Urrutia, J.A. del Valle, S. Zaefferer, D. Raabe, Study of internal stresses in a TWIP steel analyzing transient and permanent softening during reverse shear tests, J. Mater. Sci. 45 (24) (2010) 6604–6610.
- [33] A. Dumay, J.P. Chateau, S. Allain, S. Migot, O. Bouaziz, Influence of addition elements on the stacking-fault energy and mechanical properties of an austenitic Fe-Mn-C steel, Mater. Sci. Eng. A 483 (2008) 184–187.
- [34] S. Curtze, V.-T. Kuokkala, Dependence of tensile deformation behavior of TWIP steels on stacking fault energy, temperature and strain rate, Acta Mater. 58 (15) (2010) 5129–5141.
- [35] Y.F. Shen, Y.D. Wang, X.P. Liu, X. Sun, R. Lin Peng, S.Y. Zhang, L. Zuo, P.K. Liaw, Deformation mechanisms of a 20Mn TWIP steel investigated by in situ neutron diffraction and TEM, Acta Mater. 61 (16) (2013) 6093–6106.
- [36] L.V. Fricke, G. Gerstein, B. Breidenstein, H.N. Nguyen, M.A. Dittrich, H.J. Maier, D. Zaremba, Deformation-induced martensitic transformation in AlSI304 by cryogenic machining, Mater. Lett. 285 (2020) 129090–129093.
- [37] L.M. Guerrero, P.L. Roca, F. Malamud, A. Baruj, M. Sade, Experimental determination of the driving force of the fcc-hcp martensitic transformation and the stacking fault energy in high-Mn Fe-Mn-Cr steels, J. Alloys Compd. 797 (2019) 237–245.
- [38] T. Ungár, I. Dragomir, A. Révész, A. Borbély, The contrast factors of dislocations in cubic crystals: the dislocation model of strain anisotropy in practice, J. Appl. Crystallogr 32 (1999) 992–1002.
- [39] T. Ungár, J. Gubicza, P. Hanák, I. Alexandrov, Densities and character of dislocations and size-distribution of subgrains in deformed metals by X-ray diffraction profile analysis, Mater. Sci. Eng. A 319–321 (2001) 274–278.
- [40] J. Gubicza, G. Ribárik, G.R. Goren-Muginstein, A.R. Rosen, T. Ungár, The density and the character of dislocation incubic and hexagonal polycrystals determined by X-ray diffraction, Mater. Sci. Eng. A 309 (2001) 60–63.
- [41] L. Khier, L. Abdelghani, B. Okba, D. Maouche, L. Said, X-ray diffraction analysis of kaolin M1 and M2 via the Williamson-Hall and Warren-Averbach methods, J. Chem. Res. 45 (7-8) (2021) 668–673.
- [42] T. Ungár, I. Groma, M. Wilkens, Asymmetric X-ray line broadening of plastically deformed crystals. II. Evaluation procedure and ap-plication to [001]-Cu crystals, J. Appl. Cryst. 22 (1) (1989) 26–34.
 [43] T. Ungár, J. Gubicza, P. Hanák, I. Alexandrov, Densities and character of
- [43] I. Ungar, J. Gubicza, P. Hanak, I. Alexandrov, Densities and character of dislocations and size-distribution of subgrains in deformed metals by X-ray diffraction profile analysis, Mater. Sci. Eng. A 319 (2001) 274–278.
- [44] T. Ungár, S. Ott, P.G. Sanders, A. Borbély, J.R. Weertman, Dislocations, grain size and planar faults in nanostructured copper determined by high resolution X-ray diffraction and a new procedure of peak profile analysis, Acta Mater. 46 (10) (1998) 3693–3699.
- [45] B.E. Warren, B.L. Averbach, The effect of cold-work distortion on X-ray patterns, J. Appl. Phys. 21 (6) (1950) 595–599.
- [46] W.A. Bowen, P.G. Partridge, Limitations of the Hollomom strain-hardening equation, J. Phys. D: Appl. Phys. 7 (1974) 969–978.
- [47] B.E. Warren, X-Ray studies of deformed metals, Pro. Met. Phys. 8 (1959) 147–202.
- [48] T. Shintani, Y. Murata, Evaluation of the dislocation density and dislocation character in cold rolled Type 304 steel determined by profile analysis of X-ray diffraction, Acta Mater. 59 (11) (2011) 4314–4322.
- [49] K. Dutta, R. Kishor, L. Sahu, A.K. Mondal, On the role of dislocation characters influencing ratcheting deformation of austenitic stainless steel, Mater. Sci. Eng. A 660 (2016) 47–51.